

Raindrops push and splash flying insects

Andrew K. Dickerson,¹ Peter G. Shankles,¹ and David L. Hu^{2,a)}

¹*School of Mechanical Engineering, Georgia Institute of Technology, Atlanta, Georgia 30332, USA*

²*Schools of Mechanical Engineering, Biology, and Physics, Georgia Institute of Technology, Atlanta, Georgia 30332, USA*

(Received 3 May 2013; accepted 13 January 2014; published online 21 February 2014)

In their daily lives, flying insects face a gauntlet of environmental challenges, from wind gusts to raindrop impacts. In this combined experimental and theoretical study, we use high-speed videography to film raindrop collisions upon both flying insects and dynamically scaled spherical mimics. We identify three outcomes of the collision based upon the insect's mass and characteristic size: drops push the insect while remaining intact, coat the insect, and splash. We present a mathematical model that predicts impact force and outcome consistent with those found in experiments. Small insects such as gnats and flies are pushed by raindrops that remain intact upon impact; conversely, large flyers such as locusts and micro-aerial vehicles cause drops to splash. We identify a critical mass of 0.3 g for which flyers achieve both peak acceleration (100 g) and applied force (10⁴ dyn) from incoming raindrops; designs of similarly massed flying robots should be avoided. © 2014 AIP Publishing LLC. [<http://dx.doi.org/10.1063/1.4865819>]

I. INTRODUCTION

New manufacturing techniques have unleashed an array of insect-sized flying robots, also known as micro-aerial vehicles (MAVs), envisioned for use in surveillance and reconnaissance.^{1–4} Although MAVs are to be deployed outdoors, studies are generally conducted in still air rather than the complex conditions presented in nature. How can MAVs be designed to withstand in-flight perturbations from wind gusts and rain? Answering this question will help us design more robust flying robots.

Inspiration for robust and efficient flight is readily found in nature. For millions of years, flying insects have been challenged by in-flight collision with falling drops (Fig. 1). Rain of various intensity, dripping from overhanging leaves, and splashes from cascades all generate drops that may strike an insect mid-flight.^{5,6} A raindrop,⁷ like that depicted in Fig. 2, can have a mass $m_1 = 4\text{--}100$ mg, radius $R_1 = 1\text{--}4$ mm, and speed u_1 up to 10 m/s. Their shapes can vary from a sphere for small drops, to flattened shapes for large drops.

Previous studies of flight in rain focus on vertebrate flyers such as bats and birds, whose mass is much larger than raindrops. Flying bats exhibit higher metabolic consumption when flying in rain, mainly due to their additional wet mass.⁸ Hummingbirds fly in rain to feed, and can shake off accumulated water mid-flight to reduce the cost of carrying wet feathers.⁹ These animals are so large they suffer multiple raindrops in a single wingbeat. Such studies are likely not applicable to understanding how an insect flies in the rain because of the insect's much smaller size compared to vertebrate flyers.

Most flying insects are so small that falling rain appears as discrete in-flight perturbations. The mechanics of this impact is complex, and has only been studied in detail in the limit of small insect size. In 2012, Dickerson *et al.*¹⁰ showed a mosquito can survive impact with a raindrop of 50 times greater mass. The mosquito's low mass decreases its impact force by a factor of 10² relative to

^{a)} Author to whom correspondence should be addressed. Electronic mail: hu@me.gatech.edu

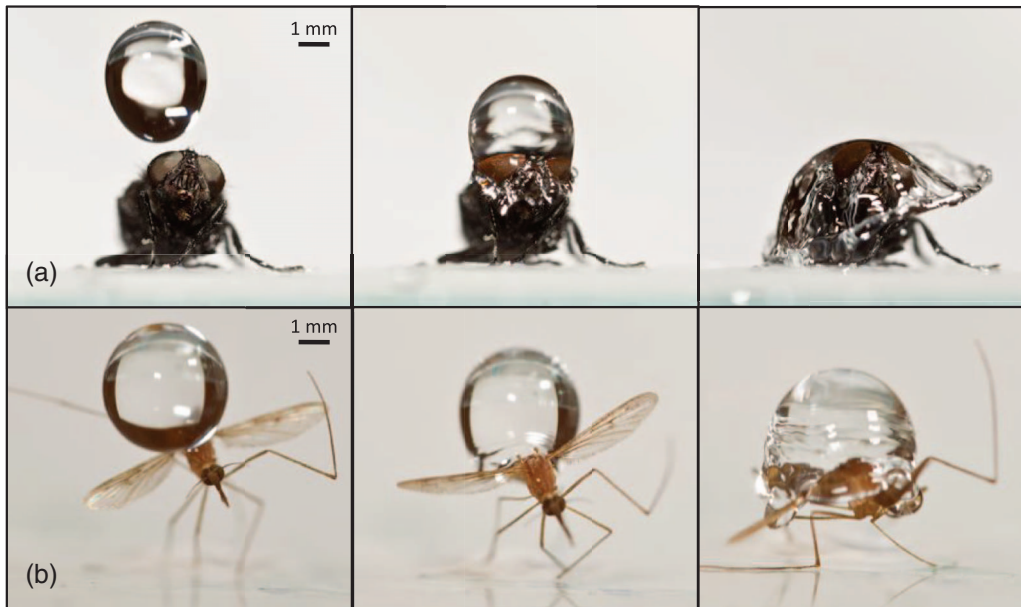


FIG. 1. Raindrop impacts upon (a) a house fly, recently deceased and standing on the ground, and (b) a live mosquito fixed to the ground.

impact on a mosquito resting on a branch.¹⁰ This study investigates how more massive insects, from a 1 mg mosquito to a 1 g dragonfly, survive impact.

Fig. 3 shows the relation between non-dimensional mass m_2/m_1 and effective radius R_2/R_1 , where R_2 is taken to be half the wingspan, of 21 insects from literature.^{11–21} We find insect wingspan scales with mass as $W \sim m_2^{0.44}$ ($R^2 = 0.91$), where mass spans 1–1200 mg and wingspan W spans 2–50 mm. In this study, we build insect mimics within this range to investigate how the size of insects affects drop collisions.

Nearly all flying insects are adapted for contact with water. Insect wings are covered with micro- and nano-scale structures which enhance hydrophobicity, enabling the wings to be cleaned more easily.²² Butterfly wings, in particular, have directional adhesion which aids in shedding drops.²³ The adaptations of these animals suggest a primal relationship between insects and rainfall.

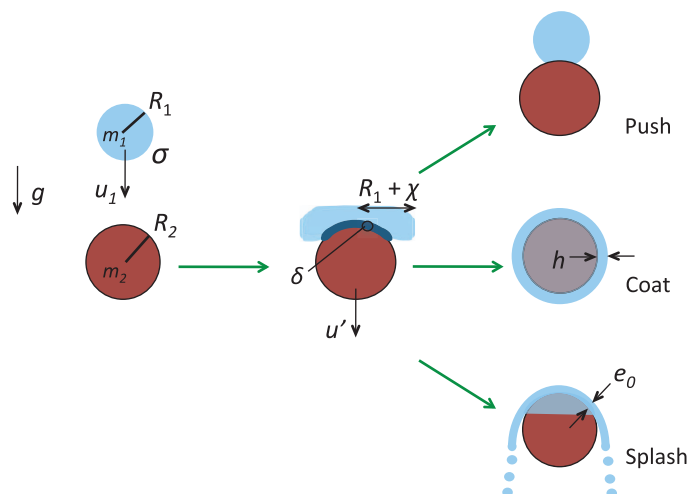


FIG. 2. Schematic diagram illustrating drop impact modes. A drop initially strikes the unsupported target, and based on the relative size and speed of the two objects, continues onward to one of three modes of impact. Here, we define variables used throughout our analysis, where δ is the boundary layer thickness upon drop deformation, χ is the increase in drop radius, h is the shell thickness of a coating drop, and e_0 is the film thickness during splashing.

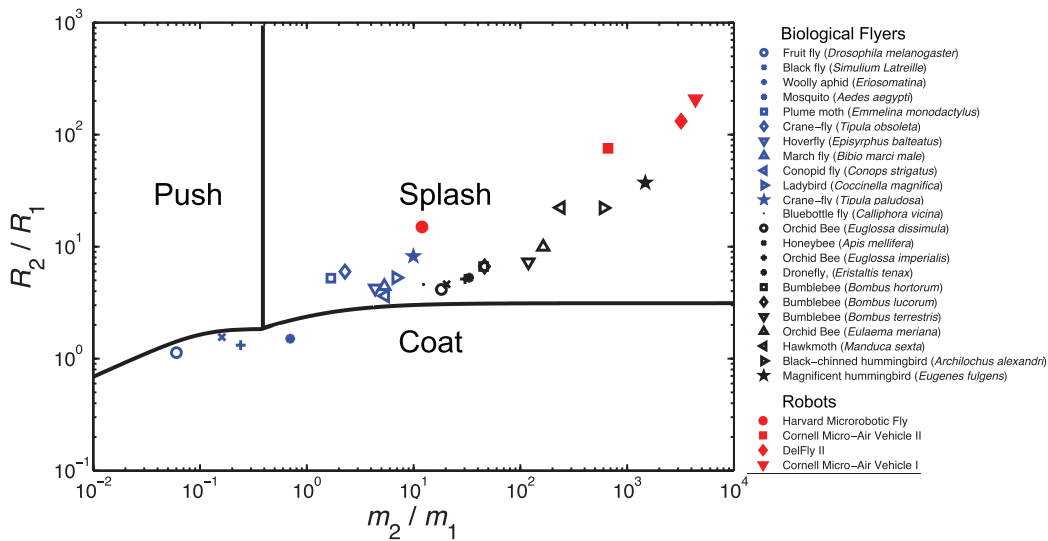


FIG. 3. The relation between radius ratio R_2/R_1 and mass ratio m_2/m_1 of insects^{11–21} and flying robots.^{1–4} Boundaries between impact modes are drawn from theory. Insects and robots are listed in order of increasing mass.

Although drop impact has been studied for decades,^{24,25} little is known regarding impact upon a small free body such as a flying insect. The closest situations to the one of interest are impact between two drops and impact between a drop and an immovable solid. In the first, several outcomes are possible, including bouncing, coalescence, disruption, and fragmentation. The resulting outcome depends exclusively on drop size, their relative velocity, and degree of offset at collision.²⁶ Other studies focus on collision of two drops of differing size, viscosity, and surface tension.²⁷ The topic of this study, the impact of a drop upon a small free body, may be considered as the impact between two drops of vastly different viscosity.

Drop impact upon an immovable solid surface may be considered as a limiting case of drop impact on a free body. As the free body grows in size to that of a large bird or aircraft, it is clear raindrops will splash upon collision. It is not yet clear, however, where the splashing threshold lies in terms of free body properties such as density, curvature, and impact speed. Drops striking solid surfaces experience one of multiple modes of impact: deposition, splashing, receding breakup, partial rebound, or complete rebound.^{25,28} Mode selection depends upon drop size, speed, impact orientation, as well as properties of the solid such as surface texture and curvature.^{29–34} Here, we clarify the onset of splashing in terms of free body properties such as density, curvature, and impact speed.

In this combined theoretical and experimental study, we investigate drop impact onto free bodies of varying mass and size. In Sec. II, we begin with our experimental methods for creating such impacts. In Sec. III, we present the observed impact outcomes and corresponding acceleration and forces applied. In Sec. IV, we proceed with a mathematical model for predicting impact outcomes. We compare these theoretical predictions to our experimental measurements in Sec. V, paying particular attention to the prediction of the impact mode outcome and impact force on biological and synthetic flyers. We discuss our theoretical simplifications and avenues for future research in Sec. VI, and summarize our conclusions in Sec. VII.

II. EXPERIMENTAL METHODS

We build 18 spherical and 10 cylindrical mimics, whose masses of 1–1000 mg and radii of 1–10 mm, are shown in Fig. 4. The mimics span the range of most flying insects (Fig. 3). In designing mimics, we neglect insect legs, wings, and wetting properties. Spherical mimics consist of an assortment of materials, including steel ball bearings, wooden beads, clay balls formed by hand, and styrofoam pellets. Additional mimics of cylindrical shape increase the mass range achievable

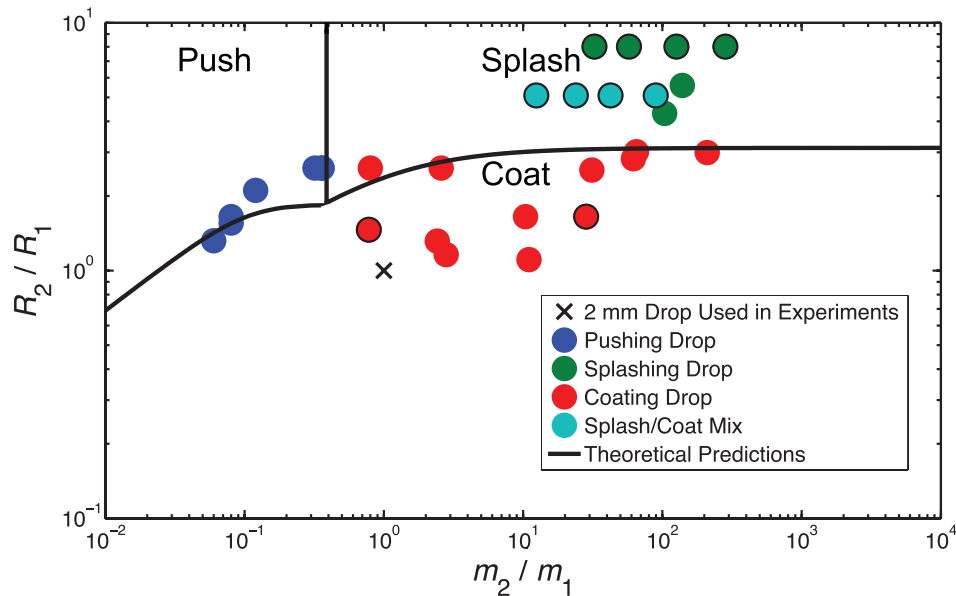


FIG. 4. The relation between radius ratio R_2/R_1 and mass ratio m_2/m_1 of insect mimics used in our experiments. Colors of data points, as listed in the legend, represent experimental observations of impact mode. Experiments are performed using a drop of radius $R_1 = 1.1$ mm depicted by the cross. Boundaries between regions are calculated using theory. Black outlines surrounding data points indicate a cylindrical mimic was used, while the data points without borders indicate a sphere was used (Multimedia view). [URL: <http://dx.doi.org/10.1063/1.4865819.1>]

by spherical mimics. Cylinder mass is easily varied by the insertion of steel or wooden cores and wrapping the outer layer of styrofoam with scotch tape. To ensure at least some similarity to filming of the spherical mimics, cylinders are filmed so that their circular cross-section faces the camera.

To mimic flight, we freely suspend mimics in the air. A drop falling from a nozzle breaks an infrared beam, causing a high-speed solenoid to retract, leaving the mimic momentarily unsupported, and poised to be struck by a drop. Details of this method are given in Dickerson *et al.*¹⁰ Mimic impacts are filmed at 1950 fps with a Phantom Miro 4C. We estimate acceleration of the mimic using the change in velocity over one video frame ($513 \mu\text{s}$). Acceleration measurements of mimics are performed at two incoming drop speeds, 2.2 m/s and 5 m/s. We combine both data sets in this study. We do not expect this variation in drop speed to substantially affect acceleration of the mimics, which varies by several orders of magnitude over the masses considered.

III. EXPERIMENTAL RESULTS

We perform a series of drop impact experiments, filmed using a high speed camera (see supplementary video multimedia view in Fig. 4 caption). Drops strike three species of live insects, mosquitoes, fruitflies, and houseflies. In addition, we film the drop impact of 28 insect spherical and cylindrical insect mimics. We categorize the impacts into three distinct modes, pushing, splashing, and coating. Fig. 4 shows the observed modes of impact, based upon the mass and size of the mimic. In this section, we introduce each of the modes and provide measurements of the impact force. For the discussion henceforth, we consider an incoming drop of mass $m_1 = 5$ mg, radius $R_1 = 1.1$ mm, and speed u_1 . Our choice of raindrop size corresponds to an average raindrop in nature.^{7,35,36} The drop collides with a spherical insect of mass m_2 and radius R_2 hovering in mid-air.

A. Pushing

Mimics of mass less than 3 mg represent the smallest insects, such as mosquitoes, blackflies, and fruit flies, which account for 20% of the mimics considered. These mimics are shown by the

TABLE I. Impact mode requirements and characteristics in relation to drop mass m_1 and radius R_1 , and target mass m_2 and radius R_2 .

Impact mode	Definition of mode	Conditions for mode		Acceleration of target	Targets	
					Insects	Mimics
Push	Drop remains intact	$m_2/m_1 \ll 1$	$R_2/R_1 \leq 1$	High	Mosquitoes, gnats	Styrofoam
Coat	Drop surrounds object	$m_2/m_1 \geq 1$	$R_2/R_1 \leq 1$	Medium - low	Tethered fruit flies	Metals
Splash	Drop fragments upon impact	$m_2/m_1 > 1$	$R_2/R_1 \gg 1$	Negligible	Bees, cicadas, dragonflies	Woods, metals

seven blue points in Fig. 4, and the insects they represent by the four leftmost symbols in Fig. 3. Such insects have less mass than raindrops, but comparable wingspan to a raindrop (Table I). Experiments in this mass range reveal that drops, surprisingly, remain intact during impact. Fig. 5(a) shows a pushing impact with a 1 mg mosquito; Fig. 5(b) shows a qualitatively similar impact with a styrofoam sphere of mass 0.6 mg.

During impact, the drop is deformed, increasing in radius as much as 80%, but still insufficient to cause breakup, which requires a radius increase³⁷ of more than 300%. The contact region of the impact remains small, constrained to the top hemisphere of the mimic. After impact, the mimic remains trapped under the drop, and relative motion ceases between the two. Neglecting aerodynamic drag, conservation of linear momentum yields the final velocity u' of the combined mass system is

$$\frac{u'}{u_1} = \left(1 + \frac{m_2}{m_1}\right)^{-1}. \quad (1)$$

Thus, the new falling speed of the combined drop-mimic is determined by the ratio of the insect mass to raindrop mass. For the smallest insects, this falling speed is often quite close to the initial raindrop speed. In this regime, fruit flies fall the fastest with 95% of the raindrop speed; mosquitoes and black flies the slowest with 80%–90% the speed. We will apply the model of inelastic impact, given in Eq. (1), as an estimate of other drop-mimic speeds in our modeling in Sec. IV.

B. Splashing

The vast majority of insects in Fig. 3 have mass 10 mg–1 g and wingspans ranging from 2 mm to 50 mm. Examples include the plume moth, crane-fly, and bumblebee. These insects are generally heavier than raindrops and have wingspans much larger than a raindrop diameter (Table I). Fig. 6(a) shows a tethered housefly which causes an impacting drop to shatter. Fig. 6(b) shows splashing on a wooden sphere, where the drop begins to break apart prior to the entire drop making contact. This

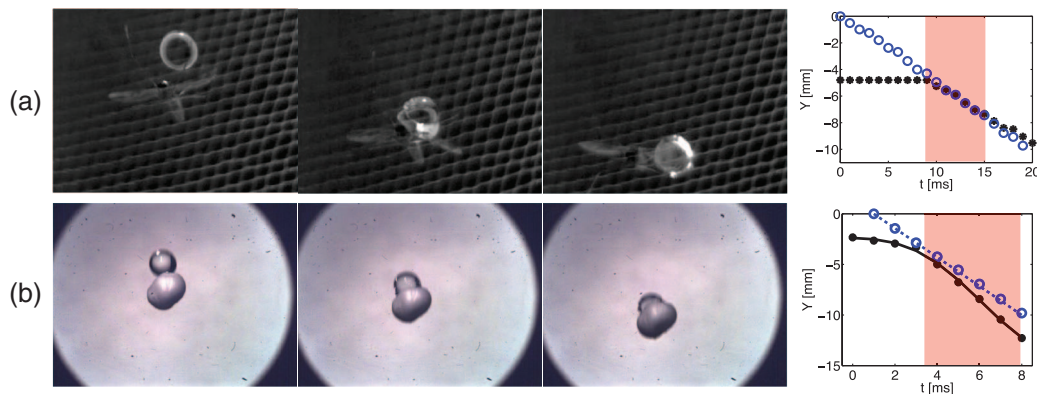


FIG. 5. Pushing: (a) A mosquito and (b) a styrofoam mimic pushed downward by a falling drop. The graphs show the time course of position of the targets (closed symbols) struck by a drop (open symbols). The shaded area denotes the duration of contact with the drop.

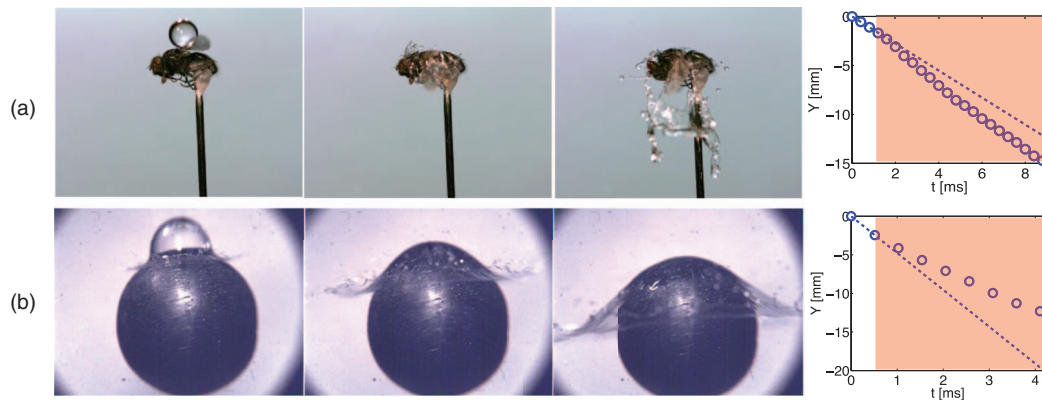


FIG. 6. Splashing: (a) A tethered housefly and (b) wooden sphere experiencing a splashing impact. Graphs (a) and (b) show the position (open symbols) of the bottom edge of a raindrop. The dashed lines show the position of mimic if no impact occurred. The pink shaded area denotes the duration of contact with the drop.

mimic is accelerated only slightly on impact. Mimics which are splashed are denoted by the green points in Fig. 4.

The largest and most massive flying creatures ($m_2/m_1 \gg 1$, $R_2/R_1 \gg 1$) will create prompt splashing producing coronas.²⁵ These include birds with masses greater than 10 g and with nearly flat surfaces (whose radii of curvature exceed 100 cm). Such impacts mimic those on unyielding surfaces and will produce impact forces greater than 50 000 dyn.¹⁰

C. Coating

Since flying insects are less dense than water, insects of comparable size to a raindrop, but heavier in mass, do not exist. For the sake of completeness, we investigated the impact of raindrops on objects of mass 1 mg–1 g but of comparable size to a raindrop (Table I). Such objects correspond to an insect standing atop a hard unyielding surface such as a branch.

One example is shown by the fruit fly tethered to a thin wire in Fig. 7(a). If the insect were untethered, a pushing impact would occur. However, the wire resists the motion of the insect, causing it to be coated by the drop. As shown by Fig. 3, most insects are too large and lightweight to be coated. Coating impacts would be maladaptive to insects because they increase the surface area in contact with the fluid.

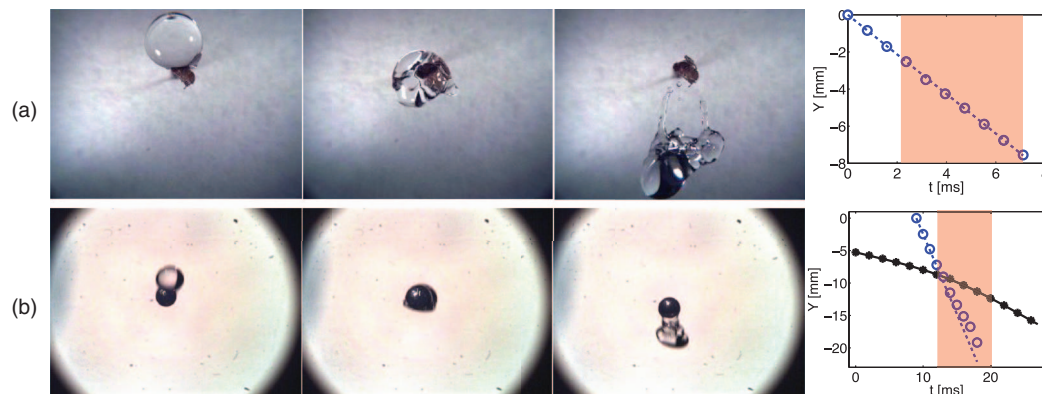


FIG. 7. Coating: (a) A fruitfly and (b) steel sphere mimic coated upon impact. Graphs (a) and (b) show the vertical position of the bottom edge of a raindrop (open symbols). Closed points show the vertical position of the mimic. The dashed lines show the position of mimic if no impact occurred.

Fig. 7(b) shows an untethered steel sphere coated by a raindrop. The drop flows around the mimic, covering its entire surface before continuing onward. During this process, the 2.2 m/s drop accelerates the mimic only slightly, increasing its velocity from 0.26 to 0.58 m/s. Most of the momentum of the drop is not transferred to the mimic, but instead flows around the target. After striking the object, the fluid re-forms into a drop, momentarily encapsulating the mimic before draining. Mimics which were coated are denoted by the red points in Fig. 4.

We further recognize a mode of impact which is a combination of splashing and coating, shown by the turquoise points in Fig. 4. In this mode, part of the drop coats the insect while part splashes, and we denote such impacts as a coating-splashing transition.

Rain is known to capture airborne particles, such as pollen and dust, as it falls.³⁸ Based on our observations, small particles impacted dead-on by raindrops will be encapsulated by a drop until collision with the ground. One of the very smallest insects, the parasitic wasp with a mass of about 0.03 mg,¹¹ would likely succumb to the same fate.

D. Impact acceleration

We rate impacts based on acceleration and impact force, which we discuss in turn. Fig. 8 shows the mimic's acceleration in terms of number of gravitational accelerations, $g = 9.81 \text{ m/s}^2$. Pushing and coating accelerates impacts by 100–400 g . The splashing region has much lower acceleration (20–50 g). This lower effectiveness of momentum transfer can be observed in the fragmented droplets, continuing downward or radially from the mimic. To give perspective on the magnitude of these accelerations, we note the human³⁹ limits for acceleration are about 50 g , the limits for fleas⁴⁰ jumping are 135 g . In comparison, impact by a falling raindrop can generate even higher accelerations.

The clear trend in Fig. 8 suggests that a scaling is possible. For impact of a drop of constant size and drop speed, we expect the acceleration a_{impact} to scale as the ratio of object's final speed u' to the impact time τ ,

$$a_{\text{impact}} = u' / \tau. \quad (2)$$

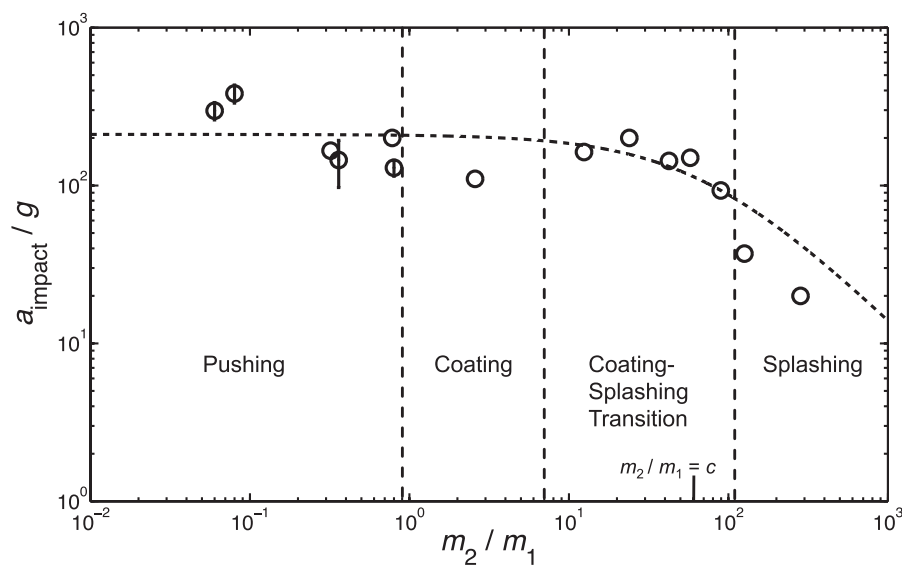


FIG. 8. The relation between acceleration in number of gravities a_{impact}/g and mass ratio m_2/m_1 , for mimics struck by drops falling at 2.2–5 m/s. The line of best fit has $R^2 = 0.45$. Delineated regions denote impact outcome, based on experimental observation.

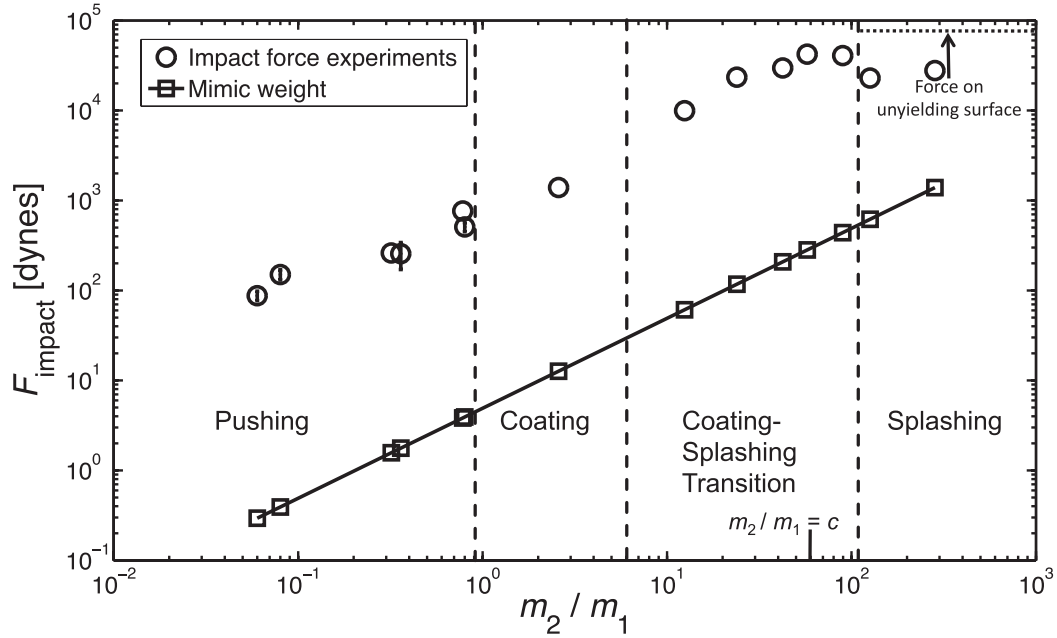


FIG. 9. The relation between impact force F_{impact} (circles) and mass ratio m_2/m_1 , for mimics struck by drops falling at 2.2–5 m/s. The relation between mimic weight (squares) and mimic mass is shown for comparison. Delineated regions denote impact outcome, based on experimental observation.

By substituting in Eq. (1) for u' , a_{impact} scales as

$$a_{\text{impact}} = \frac{1}{\tau} \frac{u_1}{1 + m_2/m_1} \sim \frac{b}{c + m_2/m_1}. \quad (3)$$

The fitting constants $b = 1.45 \times 10^5 \text{ m/s}^2$ and $c = 60$ are found using the method of least squares. Although the fit is modest ($R^2 = 0.45$), the trend line in Fig. 8 encapsulates the trends observed. For mass ratios $m_2/m_1 = 10^{-2} - 10$, which translates to $m_2 = 10^{-4} - 0.05 \text{ g}$, impact acceleration is roughly constant. After a mass ratio of 10, the acceleration decreases nonlinearly with mimic mass. In particular, an increase in mass ratio by a factor of ten from 20 to 200 causes the acceleration to decrease by a factor of five.

The magnitude of the absolute force provides further insight into the damages that a flying insect may face. Impact acceleration may easily be translated into a maximum impact force F_{impact} such that

$$F_{\text{impact}} = m_2 a_{\text{impact}}. \quad (4)$$

Fig. 9 shows the relation between maximum force F_{impact} and the mimic-drop mass ratio. Surprisingly, the trend is opposite to the acceleration trend in Fig. 8, for which the smallest mimics receive the highest acceleration. Instead, the heaviest mimics sustain the largest forces ($10^2 - 10^4 \text{ dyn}$), with the largest force at $4 \times 10^4 \text{ dyn}$. This is close to the maximum force applied by an unyielding surface, $F \sim m_1 u_1 / \tau \approx 7 \times 10^4 \text{ dyn}$. The lightest mimics sustain forces of 100 dyn, indicating that their low mass is effective in reducing the force of impact.

Based on our measurements of impact force, we observe splashing impacts are the least effective at transferring momentum. The mimics in the splashing region in Fig. 8 likely experience half of the impact acceleration they would have if the drop had remained intact. In Sec. IV, we present a mathematical model for predicting the mode of impact based on insect size and mass.

IV. MODEL

In this section, we present a theory for the mass and size range for the three distinct modes of impact, shown graphically in Fig. 2. In the push regime, the impact is inelastic, and so the kinetic energy may be easily calculated using Eq. (1). We will use this relation to calculate the conditions for the push-coat and push-splash thresholds. We seek a relation between the object mass and radius that yields an impact that is just on the border of pushing and coating. Our strategy is to use conservation of energy to yield a relation between two regimes. We use a similar method for calculating the conditions distinguishing a push from a splash impact. Finally, we consider a force balance to investigate the threshold between coating and splashing. In the theory below, this insect is assumed to be spherical for simplicity, but modifications can be made for other insect shapes.

A. Dimensionless parameters

In the following analysis of raindrop impact onto a free-flying insect, a number of dimensionless groups arise upon non-dimensionalization of our governing equations. The groups are typical of both two-body impact problems, e.g., Eq. (1), and in studies of drop impact. The groups include

$$\alpha = \frac{m_2}{m_1 + m_2} = \frac{\text{mimic mass}}{\text{combined mass}} \quad \beta = \frac{R_1}{R_2} = \frac{\text{drop radius}}{\text{mimic radius}}$$

$$\text{Re}_1 = \frac{R_1 u_1}{\nu} = \frac{\text{drop inertia}}{\text{drop viscosity}} \quad \text{We}_1 = \frac{\rho u_1^2 R_1}{\sigma} = \frac{\text{drop inertia}}{\text{drop surface tension}}. \quad (5)$$

The first two groups describe relative masses and sizes of the two bodies. The group α relates the inertia of the insect to the combined inertia of the drop-cum-insect, and emerges upon consideration of the kinetic energy before and after impact. The group β relates the relative sizes of the two objects, which is important in considering surface energy involved. Specifically, β^2 relates the surface areas of the drop to the mimic. The next two dimensionless groups are quite common in drop impact problems. Reynolds and Weber numbers for the drop size and speed considered in our model are $\text{Re}_1 = 5300$ and $\text{We}_1 = 365$, respectively, where the properties of the drop include water density $\rho = 1000 \text{ kg/m}^3$, kinematic viscosity $\nu = 10^{-6} \text{ m}^2/\text{s}$, and surface tension $\sigma = 72.8 \text{ dyn/cm}$. The Reynolds number is used in calculation of dissipated energy within the boundary layer within the drop as it strikes the mimic. The Weber number indicates the importance of the drop's inertia to capillarity. In studies of impact on unyielding surfaces, large Weber number typically indicates splashing.²⁵ However, in the case of impact on a free target of variable mass, the outcome depends on the mass and size of the object as we determine in the analysis below.

B. Push-coat threshold

We employ an energy balance on the drop before and after impact^{41,42} to predict the transition from a drop's pushing its target downward to the drop coating its target. Denoting the post-impact energy using primed notation, conservation of energy states

$$\underbrace{E_k + E_p + E_s}_{\text{before impact}} = \underbrace{E_k' + E_p' + E_s' + E_d'}_{\text{after impact}}, \quad (6)$$

where E_k , E_p , E_s , and E_d are kinetic, potential, surface, and dissipative energies, respectively. Mass conservation dictates the mass of the drop remains unchanged throughout the impact: namely, $m_1 = m_1'$. We take $E_p = E_p'$ by assuming the drop does not substantially change in elevation with respect to the target just prior to and after the collision.

At the border of coating and pushing, the impact is inelastic and the drop surrounds a spherical target and remains adhered as in Fig. 2. Initial kinetic and surface energies, E_k and E_s , remain unchanged for all impacts. We calculate E_s' and E_d' based upon the lowest-energy coating scenario, considering the flows that occur as the drop deforms from a sphere to a spherical shell coating the mimic. At conditions away from this threshold, the assumptions we have made about drop

deformation and impact kinetics become inaccurate. We therefore define a term which captures the error in our calculation of the energy balance in Eq. (6), given by

$$\Delta E = E_k + E_s - E'_k - E'_s - E'_d. \quad (7)$$

The sign of ΔE determines which impact mode will be witnessed. During pushing, the drop does not form a complete spherical shell around the mimic, and so our method overestimates the surface E'_s , and dissipative E'_d , energies. Thus, we expect the error ΔE to be negative if the impact is a push. Conversely, a faster incoming drop would flow around the target and continue past it as in Fig. 7. This would lead to more residual kinetic energy E'_k than that calculated using an inelastic impact, and so an underestimated E'_k . Thus, we expect the error ΔE to be positive if the impact is a coat. Together, our relation for distinguishing pushing from coating is

$$\Delta E \begin{cases} < 0 & \text{push} \\ > 0 & \text{coat.} \end{cases} \quad (8)$$

To complete this analysis, we now write relations for all the terms in Eq. (7). The initial kinetic and surface energies of the system may be written as that of a spherical drop,

$$E_k = \frac{1}{2} m_1 u_1^2, \quad (9)$$

$$E_s = 4\pi\sigma R_1^2. \quad (10)$$

These energies are converted into several terms throughout the impact process, including the final kinetic and surface energies of the drop-cum-mimic, and the irrecoverable dissipation during impact. We now estimate these final energies of the system post-impact.

The final kinetic energy is estimated as that for inelastic impact,

$$E'_k = E_{k,\text{inelastic}} = \frac{1}{2} (m_1 + m_2) (u')^2, \quad (11)$$

where we use Eq. (1) to substitute for u' . This equation represents the greatest possible kinetic energy change for the system, as inelastic impact slows the drop more than other impact types. This estimate will be accurate for pushing, but will be an underestimate for high-speed coating flows in which the fluid continues flowing past the mimic.

We write the final surface energy as that associated with a spherical shell surrounding its target as illustrated by Fig. 2. This surface energy is comprised of the energy in the solid-liquid surface and the air-liquid surface,

$$E'_s = \underbrace{4\pi\sigma R_2^2 (1 - \cos\theta)}_{\text{solid-liquid surface}} + \underbrace{4\pi\sigma (R_1^3 + R_2^3)^{\frac{2}{3}}}_{\text{air-liquid surface}}, \quad (12)$$

where θ is the contact angle of water on the target.

Viscous dissipation arises from the drop's deformation upon impact. The time-scale of deformation is $\tau \approx 2R_1/(u_1 - u')$. To calculate dissipation, we apply a method, by Pasandideh-Fard⁴¹ and Mundo,⁴² for estimating dissipation during impact of drops onto flat surfaces. Dissipation occurs as the fluid undergoes shear within the boundary layer. Using stagnation point flow, this layer can be estimated to be of thickness⁴¹ $\delta = 4R_1/\sqrt{\text{Re}}$, where the Reynolds number $\text{Re} = R_1(u_1 - u')/\nu$. The viscous dissipation per unit mass³⁴ is $\Phi = \mu \left(\frac{\partial v_i}{\partial x_j} + \frac{\partial v_j}{\partial x_i} \right) \frac{\partial v_i}{\partial x_j} \approx \rho\nu(u_1 - u')^2/\delta^2$.

The volume of the boundary layer is approximated by considering the deformation of a drop into a spherical shell that encapsulates the impacted object. At the end of the impact, the drop assumes a spherical shell of thickness $h = (R_1^3 + R_2^3)^{\frac{1}{3}} - R_2$. We model this process as the flattening of a drop of radius R_1 to $R_{\text{max}} = \sqrt{4R_2^3/3h}$, where R_{max} is the effective radius of a disc of height h and the original volume of the drop. The volume of fluid over which dissipation takes place is approximated

by $\Omega \approx \pi R_{\max}^2 \delta$. The total dissipation, E'_d , within the drop is

$$E'_d = \int_0^\tau \int_\Omega \Phi \, d\Omega \, dt \approx \Phi \Omega \tau. \quad (13)$$

The energy lost due to viscous dissipation may be approximated by substituting Φ , Ω , and τ into Eq. (13), yielding

$$E'_d = \frac{1}{2} \rho \nu \pi R_{\max}^2 (u_1 - u') \sqrt{\text{Re}}. \quad (14)$$

By substituting Eqs. (9)–(12) and (14) into Eq. (6) and rearranging, we arrive at

$$\begin{aligned} \Delta E = \frac{1}{2} [m_1 u_1^2 - (m_1 + m_2) (u')^2] + 4\pi \sigma [R_1^2 - R_2^2 (1 - \cos \theta) - (R_1^3 + R_2^3)^{\frac{2}{3}}] \\ - \frac{1}{2} \rho \nu \pi R_{\max}^2 (u_1 - u') \sqrt{\text{Re}}, \end{aligned} \quad (15)$$

where m_2 and R_2 are the only non-constant terms.

We may non-dimensionalize Eq. (15) by dividing by $\rho \pi u_1^2 R_1^3$, yielding a dimensionless energy

$$\Delta E^* = \alpha \left[1 - \frac{(\text{Re}_1)^{-\frac{1}{2}}}{\beta(\beta^3 + 1)^{\frac{1}{3}} - \beta} \right] + \frac{6}{\text{We}_1} [\cos \theta - (1 + \beta)^{\frac{2}{3}}], \quad (16)$$

where α and β are defined in Eq (5) and our push-coat criterion is

$$\Delta E^* \begin{cases} < 0 & \text{push} \\ > 0 & \text{coat.} \end{cases} \quad (17)$$

Equations (16) and (17) are physically consistent in light of limits of dimensionless groups involved. Note the second term in Eq. (16) is negative because $0^\circ < \theta < 180^\circ$. Thus, for very low inertia or very high surface tension, $\text{We}_1 \rightarrow 0$, ΔE^* decreases, indicating that pushing the target is now favorable. In the limits of either high viscosity, $\text{Re}_1 \rightarrow 0$, or for superhydrophobic targets, $\cos \theta \rightarrow -1$, the dimensionless energy ΔE^* decreases, promoting pushing. We plot the curve given by Eq. (16) in Fig. 4 to predict the threshold between pushing and coating, by specifying values of m_2/m_1 and plotting values of R_2/R_1 for which $\Delta E^* = 0$. No free parameters are employed in computing the push-coat transition Eq. (15).

C. Push-splash threshold

In Sec. IV B, we determine the threshold between the push and coat modes. In coating, we assume the drop completely coats its spherical target. In this section, we use observations from our experiments to make several modifications to this physical picture to consider splashing. First, more residual kinetic energy remains in splashing than in coating at the end of the impact. Second, splashing coats the target less than a coating impact.

In this section, we calculate the final kinetic energy E'_k using an inelastic impact model, and the final surface E'_s and dissipative E'_d energies using a model for drop deformation, or flattening, upon impact. If the drop's initial kinetic E_k and surface E_s energies are too high to be absorbed into surface energy and dissipation, the drop will splash. Our model for E'_k , E'_s , and E'_d becomes invalid if the drop breaks apart, but remains valid if the drop stays intact.

We begin with Eq. (13) as before, but consider instead the boundary layer volume $\Omega \approx \pi (R_1 + \chi)^2 \delta$ occupied by a disk of radius $R_1 + \chi$ and height δ . We apply a method we previously used to model the deformation of a drop upon a sphere.¹⁰ Impact increases the radius R_1 by an amount χ ,

$$\frac{\chi}{R_1} \sim \sqrt{\text{We}_1} \left(\frac{m_1}{m_2} + 1 \right)^{-1}. \quad (18)$$

A more detailed derivation of Eq. (18) may be found in Dickerson *et al.*¹⁰ For the remainder of this section, we use a scaling factor of unity in Eq. (18); this scaling factor will be used as a free parameter when we compare our theory to experiment in Section V. Combining Eq. (18) with Eq. (13), and now using $R_1 + \chi$ in place of R_{\max} to determine the volume of dissipating fluid Ω , we arrive at the dissipation

$$E'_d \approx \Phi \Omega \tau \sim \frac{1}{2} \rho \nu \pi (R_1 + \chi)^2 (u_1 - u') \sqrt{\text{Re}}. \quad (19)$$

Assuming the drop flattens into a disc upon impact, we estimate the final surface energy as the sum of the solid-liquid energy and the air-liquid energy,

$$E'_s = \pi \sigma (R_1 + \chi)^2 (2 - \cos \theta). \quad (20)$$

Combining Eqs. (9)–(11) and (18)–(20) for the push-splash threshold, we may rewrite Eq. (7) as

$$\begin{aligned} \Delta E = \frac{1}{2} [m_1 u_1^2 - (m_1 + m_2)(u')^2] + \pi \sigma [4R_1^2 - (R_1 + \chi)^2 (2 - \cos \theta)] \\ - \frac{1}{2} \rho \nu \pi (R_1 + \chi)^2 (u_1 - u') \sqrt{\text{Re}}, \end{aligned} \quad (21)$$

where m_2 is the only non-constant term.

We may non-dimensionalize Eq. (15) by dividing by $\rho \pi u_1^2 R_1^3$, yielding a dimensionless energy

$$\Delta E^* = \frac{2}{3} \alpha + \frac{4}{\text{We}_1} - \left(1 + 2\alpha \sqrt{\text{We}_1} + \alpha^2 \text{We}_1\right) \left[\frac{2 - \cos \theta}{\text{We}_1} + \frac{\alpha^{3/2}}{2\sqrt{\text{Re}_1}} \right], \quad (22)$$

and our push-splash criteria as

$$\Delta E^* \begin{cases} < 0 & \text{splash} \\ > 0 & \text{push.} \end{cases} \quad (23)$$

In Eq. (22), we can reason that as m_1 increases, the corresponding decrease in the combined mass ratio α will increase ΔE^* , promoting pushing. This is consistent with our experiments, in which decreasing m_2/m_1 produces smaller drop deformations and subsequently, pushing.¹⁰ Similarly, as the target becomes more hydrophobic, $\cos \theta \rightarrow -1$, ΔE^* will decrease, promoting splashing. We plot the vertical line given by Eq. (22) in Fig. 4 to predict the threshold between pushing and splashing, by specifying values of m_2/m_1 for which $\Delta E^* = 0$. Unlike Sec. IV B, the energy balance given in Eqs. (21) and (22) has no dependence on R_2/R_1 . Such a result occurs because we assume drop deformation is unaffected by mimic size in Eq. (18). We justify this approximation in the regime in which mimic radius exceeds drop radius ($R_2/R_1 > 2$), which is the region of interest, as shown in Fig. 4.

D. Coat-splash threshold

At the threshold of coating and splashing, the drop deforms beyond a point where pushing is possible. The drop flattens sufficiently that it forms a thin film on the top of the target, after which two outcomes can occur: it can remain adhered, creating a coat, or shed off in a ligament or drops, creating a splash. Consideration of attachment or separation from the target's curved surface is a solved problem called the teapot effect.⁴³ To determine the conditions for distinguishing a coat from a splash, we consider a force balance between inertial and adhesive forces for the flow around a curved surface.⁴⁴

Duez *et al.*⁴⁴ report a critical Weber scaling that characterizes the transition between fluid attachment and separation. We apply their theory using the relative velocity between drop and mimic, $u_1 - u'$, and the length scale given by the film thickness $e_0 \simeq R_1^2/2R_2$, estimated from the

Bernoulli equation, to define a Weber number,

$$\text{We}^* = \frac{\rho(u_1 - u')^2 e_0}{\sigma}. \quad (24)$$

A radial force balance equates centrifugal forces with the adhesion forces of the fluid to the sphere. This force balance can be written in non-dimensionalized form

$$\text{We}^* \propto \frac{R_2^2}{e_0^2} (1 + \cos \theta). \quad (25)$$

During splashing, inertial forces dominate and so Weber number is above the critical value above. Thus,

$$\text{We}^* \begin{cases} < R_2^2 (1 + \cos \theta) / e_0^2 & \text{coat} \\ > R_2^2 (1 + \cos \theta) / e_0^2 & \text{splash.} \end{cases} \quad (26)$$

By equating expressions for We^* given by Eqs. (24)–(26), we write the condition for splashing,

$$R_2 < \left[\frac{\rho R_1^6 (u_1 - u')^2}{\sigma (1 + \cos \theta)} \right]^{\frac{1}{5}}. \quad (27)$$

We may non-dimensionalize Eq. (27) by dividing by $\rho \pi u_1^2 R_1^3$, yielding a radius ratio

$$\frac{R_2}{R_1} < \left[\frac{\alpha^2 \text{We}_1}{(1 + \cos \theta)} \right]^{\frac{1}{5}}. \quad (28)$$

A drop with a very high initial velocity, producing a large We_1 , and a target with a hydrophobic surface such that $\cos \theta \rightarrow -1$, promotes splashing by increasing the right-hand-side of Eq. (28). We plot the curve specified by the threshold given in Eq. (28) by specifying values of m_2/m_1 and plotting values of R_2/R_1 , which satisfy the equality. No scaling coefficient was required to shift the curve to the intersection of the curves plotted by Eqs. (16) and (22).

V. COMPARISON OF THEORY TO EXPERIMENT

Previously, we presented implicit equations, Eqs. (16), (22), and (28), for the mass-radius coordinates of each impact mode. We use Mathematica to numerically solve these equations by inputting a mass ratio m_2/m_1 and calculating a corresponding radius ratio R_2/R_1 which solves the equations. Although insects are hydrophobic, we perform experiments with hydrophilic mimics. Thus, we assume in our calculations that the contact angle of water on the mimics is $\theta = 80^\circ$.

We have freedom to choose where to terminate each curve, and so we terminate curves given by Eqs. (16) and (22) at their point of intersection. For the push-splash transition, in Eq. (18), we use a free parameter of 0.7 to shift the curve given by Eq. (22), such that the curve segregates our experimental data points appropriately. As shown in Fig. 4, our theoretical predictions for impact mode match well our experimental observations. Only a few points stray from their predicted zones. We proceed to use our findings to predict impact phenomenon on organisms.

A. Predictions for insects and flying robots

Fig. 3 shows the predicted impact modes for various insects. The model predicts that insects above 100 mg will splash, which seems quite feasible. Inaccuracies are due to our modeling the insect wing, which is flat, as a curved surface. Consequently, the smallest insects lie at the coating-pushing border rather than within the push regime. Mosquitoes in particular are known to be pushed by raindrops.¹⁰ Another inaccuracy is in the coat regime: four insects lie just within the coat regime rather than within the push regime.

We apply our model to predict the effects of raindrop impact on flying robots. We consider four robots, including Harvard's Microrobotic Fly, Cornell's Micro-Air Vehicles I-II, and the Delfly,¹⁻⁴ whose mass and half their wingspan is given in Fig. 3. All robots are within the splashing zones.

Pushing is not possible, as the robots are 2–4 orders of magnitude too heavy, and 1–2 orders of magnitude too large. Most would need radii two orders of magnitude less than their current values to be in danger of coating. The Harvard microrobotic fly is most in danger of coating: if its wingspan were 3 mm rather than 1 cm, its wings would be coated by the drop. In fact, it is likely that parts of the body which are more slender than the wings will be coated if they are struck by a drop.

B. Acceleration and force resistance for small and large insects

We now consider the effects of scaling on raindrop impact. Scaling is particularly useful as flying insect masses range over 6 orders of magnitude, and synthetic flyers span an additional order of magnitude.

We consider two regimes, the limit of very lightweight and very heavy insects. Small insects have an impressive ability to survive very large accelerations. For example, fleas can survive 135 *g* during jumping, and a mosquito 300 *g* during raindrop impact.¹⁰ This increasing tolerance to acceleration at small sizes can be explained using scaling.

Fig. 3 shows that impact accelerations a_{impact}/g asymptote to a constant value of 250 for small sizes. This value arises from consideration of Eq. (3), for which the acceleration due to drop impact, $a_{\text{impact}} \approx \frac{b}{c+m_2/m_1} = \frac{b/c}{1+m_2/cm_1}$. For small insects, which have a mass $m_2 \ll cm_1 = 0.3$ g, the acceleration due to drop impact approaches a constant, $b/cg \approx 250$. Although this acceleration is high, smaller insects, are relatively more capable of surviving accelerations. This increasing strength at small sizes is due to the strength scaling of materials, observed first by Leonardo da Vinci, and reported by McMahon⁴⁵ and Schmidt-Nielsen.⁴⁶ Materials of the same composition have a constant yield stress, and so the maximum force F_{material} a material can withstand scales as its cross-sectional area, $F_{\text{material}} \sim m_2^{2/3}$. Using Newton's second law, $F_{\text{material}} = m_2 a_{\text{material}}$, the impact acceleration a material can withstand scales as $a_{\text{material}} \sim m_2^{-1/3}$. As insects become smaller, the maximum acceleration a material can withstand will exceed that provided by a raindrop: $a_{\text{material}} > a_{\text{impact}}$. Thus, smaller insects are invincible with respect to acceleration caused by drop.

As insects increase in size, the force of raindrop impact becomes small compared to both the insect weight and the force their materials can withstand. Fig. 9 shows that as an insect grows larger, the force from a raindrop asymptotes to a constant value of 10^4 dyn. This results from consideration of Eq. (4), for which the force due to drop impact, $F_{\text{impact}} \approx \frac{bm_2}{c+m_2/m_1} = \frac{bm_2m_1}{cm_1+m_2}$. For large insects, which have a mass $m_2 \gg cm_1 = 0.3$ g, the force due to drop impact F_{drop} approaches a constant, $bm_1 \approx 7 \times 10^4$ dyn. This scaling is adaptive for larger insects, which become relatively more capable of surviving force. The force of raindrop impact will be exceeded by both an insect's weight, scaling as m_2 , and the force its materials can withstand, which scale as $m_2^{2/3}$. A small bird with mass $m_2 = bm_1/g = 74$ g receives an impact force equal to its weight. A Ladybird of mass 2 g receives an impact force 1/10 of its weight.

VI. DISCUSSION

Our experiments involve several assumptions and simplifications which we review here. Since fast drops cannot be easily aimed at our mimics, we employ drops of speed $u_1 = 2.2\text{--}5$ m/s, which is 45%–75% slower than a terminal-velocity raindrop. Experiments conducted with terminal raindrops would produce modifications to regimes in Fig. 4. Specifically, coating and splashing would occur for lower radius R_2 and mass m_2 values. In addition, the acceleration and force on an insect will increase (Fig. 9), as a greater amount of momentum is available for transfer to the object. Finally, we assume only spherical drops of fixed size. However, as discussed by Reyssat,⁷ raindrops have a range of size and shape. In particular, our transition lines in Fig. 4 may not be robust to changes in drop shape.

Wings and legs increase the force of raindrop impact by increasing the insect's aerodynamic resistance. During the high accelerations applied, these structures provide added mass to the insect and shift points to the right in Figs. 3 and 4. Insects with the largest wings for their size such as butterflies will experience the greatest deviation from the predicted trends. Wings induce splashing at mass values smaller than predicted in Fig. 3.

Behavior of the insect will not likely influence impact force. The maximum speeds of most insects is less than 10 m/s, the terminal speed of a falling raindrop.⁴⁷ Even at slow flight speeds, however, the formation of a boundary layer as a result of wing motion may help to dispel the smallest drops. For instance, it is known the boundary layers formed on discs spinning at exceedingly high speed may prevent drops from impacting the surface.⁴⁸

In this study, we consider the impact outcome of a raindrop striking an insect. Conversely, one might consider the fate of the insect during impact: does it fragment or splash upon striking an incoming object? From our experiments and theoretical analysis in Sec. V B, we conclude that an insect will not break apart from the force of a raindrop impact. However, as we know from common experience, insect splashing does occur upon impact with automobiles. This splashing is due to the high impact force imparted by the high momentum of the automobile. For example, if a 2-mg mosquito is struck by an automobile traveling at 15 mph = 6.7 m/s, it will experience an impact force of 9000 dyn, which is comparable to the force required to kill a mosquito. Larger insects may even splash. If that same car strikes a 1-cm long 0.3 g insect, which is 150 times heavier than a mosquito, the insect will experience an impact force of 240 000 dyn. A car traveling at higher speeds would generate even higher impact forces, which explains why a car driving at 50 mph is often covered with dead splattered insects.

VII. CONCLUSION

We perform raindrop impact experiments on free-falling insects and their mimics. By systematically varying the size and mass of the mimics, we observe three distinct impact modes which we refer to as pushing, splashing, and coating. In our supporting theoretical study, we derive mathematical relations for the regime of object mass and size associated with each impact mode. These regimes are consistent with our experimental observations. The push-coat and push-splash transitions are determined from consideration of energetics, whereas the coat-splash transition is determined from the balance of centrifugal and adhesive forces.

Our study shows how flying in the rain is strongly affected by body size. Our lightest mimics experience the highest impact accelerations of 300 *g*, but the lowest absolute forces of 100 dyn. Conversely, the heaviest mimics experience the lowest accelerations of 20 *g*, but the highest impact forces of 4×10^4 dyn. Based on our experiments with both mimics and insects, we predict insects smaller than 2 mg are pushed by raindrops, whereas larger insects cause raindrops to splash. Consequently, a modern MAV causes raindrops to splash, and should be designed to withstand this force and to contend with splashes shed on its body.

We also identify a sub-optimal size for which objects are most poorly suited for dealing with rain. Objects experience both peak acceleration and peak force at a critical mass of 0.3 g, about the weight of a bumblebee. Biological organisms and synthetic flyers should avoid this mass if they are to minimize acceleration and force due to rain.

ACKNOWLEDGMENTS

We thank Nihar Madhavan for his early experimental contributions and National Science Foundation (NSF) CAREER (PHY-1255127) for financial support.

- ¹R. Wood, "The first takeoff of a biologically inspired at-scale robotic insect," *IEEE Trans. Robotics* **24**, 341–347 (2008).
- ²G. De Croon, K. De Clercq, R. Ruijsink, B. Remes, and C. De Wagter, "Design, aerodynamics, and vision-based control of the DelFly," *Int. J. Micro Air Vehicles* **1**, 71–97 (2009).
- ³C. Richter and H. Lipson, "Untethered hovering flapping flight of a 3D-printed mechanical insect," *Artif. Life* **17**, 73–86 (2011).
- ⁴F. Van Breugel, Z. Teoh, and H. Lipson, "A passively stable hovering flapping micro-air vehicle," *Flying Insects and Robots* (Springer, 2010), pp. 171–184.
- ⁵G. J. Amador, Y. Yamada, M. McCurley, and D. L. Hu, "Splash-cup plants accelerate raindrops to disperse seeds," *J. R. Soc. Interface* **10**, 0880 (2013).
- ⁶D. Attenborough, *Life in the Undergrowth* (BBC One, 2005).
- ⁷E. Reyssat, F. Chevy, A.-L. Biance, L. Petitjean, and D. Quéré, "Shape and instability of free-falling liquid globules," *Europhys. Lett.* **80**, 34005 (2007).

- ⁸ C. Voigt, K. Schneeberger, S. Voigt-Heucke, and D. Lewanzik, "Rain increases the energy cost of bat flight," *Biol. Lett.* **7**, 793–795 (2011).
- ⁹ V. Ortega-Jimenez and R. Dudley, "Aerial shaking performance of wet Anna's hummingbirds," *J. R. Soc. Interface* **9**, 1093–1099 (2011).
- ¹⁰ A. K. Dickerson, P. G. Shankles, N. M. Madhavan, and D. L. Hu, "Mosquitoes survive raindrop collisions by virtue of their low mass," *Proc. Natl. Acad. Sci. U.S.A.* **109**, 9822–9827 (2012).
- ¹¹ T. Weis-Fogh, "Quick estimates of flight fitness in hovering animals, including novel mechanisms for lift production," *J. Exp. Biol.* **59**, 169–230 (1973).
- ¹² A. R. Ennos, "The kinematics and aerodynamics of the free flight of some Diptera," *J. Exp. Biol.* **142**, 49–85 (1989).
- ¹³ S. N. Fry, R. Sayaman, and M. H. Dickinson, "The aerodynamics of hovering flight in *Drosophila*," *J. Exp. Biol.* **208**, 2303–2318 (2005).
- ¹⁴ C. Ellington, "The aerodynamics of hovering insect flight. III. Kinematics," *Philos. Trans. R. Soc. London, Ser. B* **305**, 41–78 (1984).
- ¹⁵ C. Ellington, "The aerodynamics of hovering insect flight. II. Morphological parameters," *Philos. Trans. R. Soc. London, Ser. B* **305**, 17–40 (1984).
- ¹⁶ Y. Liu and M. Sun, "Wing kinematics measurement and aerodynamics of hovering droneflies," *J. Exp. Biol.* **211**, 2014–2025 (2008).
- ¹⁷ R. Dudley, "Extraordinary flight performance of orchid bees (Apidae: Euglossini) hovering in heliox (80% He/20% O₂)," *J. Exp. Biol.* **198**, 1065–1070 (1995).
- ¹⁸ R. Dudley and C. Ellington, "Mechanics of forward flight in bumblebees: I. Kinematics and morphology," *J. Exp. Biol.* **148**, 19–52 (1990).
- ¹⁹ A. P. Willmott and C. P. Ellington, "The mechanics of flight in the hawkmoth *manduca sexta*. II. Aerodynamic consequences of kinematic and morphological variation," *J. Exp. Biol.* **200**, 2723–2745 (1997).
- ²⁰ A. P. Willmott and C. P. Ellington, "The mechanics of flight in the hawkmoth *Manduca sexta*. I. Kinematics of hovering and forward flight," *J. Exp. Biol.* **200**, 2705–2722 (1997).
- ²¹ P. Chai and D. Millard, "Flight and size constraints: Hovering performance of large hummingbirds under maximal loading," *J. Exp. Biol.* **200**, 2757–2763 (1997).
- ²² D. Byun *et al.*, "Wetting characteristics of insect wing surfaces," *J. Bionic Eng.* **6**, 63–70 (2009).
- ²³ Y. Zheng, X. Gao, and L. Jiang, "Directional adhesion of superhydrophobic butterfly wings," *Soft Matter* **3**, 178–182 (2007).
- ²⁴ E. Villermaux, B. Bossa *et al.*, "Drop fragmentation on impact," *J. Fluid Mech.* **668**, 412–435 (2011).
- ²⁵ A. Yarin, "Drop impact dynamics: Splashing, spreading, receding, bouncing . . .," *Annu. Rev. Fluid Mech.* **38**, 159–192 (2006).
- ²⁶ Y. Jiang, A. Umemura, and C. Law, "An experimental investigation on the collision behaviour of hydrocarbon droplets," *J. Fluid Mech.* **234**, 171–190 (1992).
- ²⁷ M. Orme, "Experiments on droplet collisions, bounce, coalescence and disruption," *Prog. Energy Combust. Sci.* **23**, 65–79 (1997).
- ²⁸ M. Rein, "Phenomena of liquid drop impact on solid and liquid surfaces," *Fluid Dyn. Res.* **12**, 61–93 (1993).
- ²⁹ J. Field, J. Dear, and J. Ogren, "The effects of target compliance on liquid drop impact," *J. Appl. Phys.* **65**, 533–540 (1989).
- ³⁰ S. Bakshi, I. Roisman, and C. Tropea, "Investigations on the impact of a drop onto a small spherical target," *Phys. Fluids* **19**, 032102 (2007).
- ³¹ A. Rozhkov, B. Prunet-Foch, and M. Vignes-Adler, "Dynamics of a liquid lamella resulting from the impact of a water drop on a small target," *Proc. R. Soc. London, Ser. A* **460**, 2681 (2004).
- ³² A. Rozhkov, B. Prunet-Foch, and M. Vignes-Adler, "Impact of water drops on small targets," *Phys. Fluids* **14**, 3485 (2002).
- ³³ M. Bussmann, J. Mostaghimi, and S. Chandra, "On a three-dimensional volume tracking model of droplet impact," *Phys. Fluids* **11**, 1406 (1999).
- ³⁴ S. Chandra and C. Avedisian, "On the collision of a droplet with a solid surface," *Proc. Math. Phys. Sci.* **432**, 13–41 (1991).
- ³⁵ D. Hauser, P. Amayenc, B. Nutten, and P. Waldteufel, "A new optical instrument for simultaneous measurement of raindrop diameter and fall speed distributions," *J. Atmos. Oceanic Technol.* **1**, 256–269 (1984).
- ³⁶ R. Gunn and G. Kinzer, "The terminal velocity of fall for water droplets in stagnant air," *J. Meteorol.* **6**, 243–248 (1949).
- ³⁷ C. Clanet, C. Béguin, D. Richard, and D. Quéré, "Maximal deformation of an impacting drop," *J. Fluid Mech.* **517**, 199–208 (2004).
- ³⁸ J. E. McDonald, "Collection and washout of airborne pollens and spores by raindrops," *Science* **135**, 435–437 (1962).
- ³⁹ J. P. Stapp, "Effects of mechanical force on living tissues," *J. Aviation Med.* **26**, 268 (1955).
- ⁴⁰ H. Bennet-Clark and E. Lucey, "The jump of the flea: A study of the energetics and a model of the mechanism," *J. Exp. Biol.* **47**, 59–76 (1967).
- ⁴¹ M. Pasandideh-Fard, Y. Qiao, S. Chandra, and J. Mostaghimi, "Capillary effects during droplet impact on a solid surface," *Phys. Fluids* **8**, 650 (1996).
- ⁴² C. Mundo, M. Sommerfeld, and C. Tropea, "Droplet-wall collisions: Experimental studies of the deformation and breakup process," *Int. J. Multiphase Flow* **21**, 151–173 (1995).
- ⁴³ J. Keller, "Teapot effect," *J. Appl. Phys.* **28**, 859–864 (1957).
- ⁴⁴ C. Duez, C. Ybert, C. Clanet, and L. Bocquet, "Wetting controls separation of inertial flows from solid surfaces," *Phys. Rev. Lett.* **104**, 084503 (2010).
- ⁴⁵ T. A. McMahon and J. T. Bonner, *On Size and Life* (Scientific American Books, New York, NY, 1983).
- ⁴⁶ K. Schmidt-Nielsen, *Scaling* (Cambridge University Press, New York, NY, 1984).
- ⁴⁷ C. Ellington, "Limitations on animal flight performance," *J. Exp. Biol.* **160**, 71–91 (1991).
- ⁴⁸ O. Povarov, O. Nazarov, L. Ignat'evskaya, and A. Nikol'skii, "Interaction of drops with boundary layer on rotating surface," *J. Eng. Phys. Thermophys.* **31**, 1453–1456 (1976).